The Force Needed to Move an Atom on a Surface

Markus Ternes,[1]† Christopher P. Lutz,[1] Cyrus F. Hirjibehedin,[1]*
Franz J. Giessibl,[2] Andreas J. Heinrich[1]

Manipulation of individual atoms and molecules by scanning probe microscopy offers the ability of controlled assembly at the single-atom scale. However, the driving forces behind atomic manipulation have not yet been measured. We used an atomic force microscope to measure the vertical and lateral forces exerted on individual adsorbed atoms or molecules by the probe tip. We found that the force that it takes to move an atom depends strongly on the adsorbate and the surface. Our results indicate that for moving metal atoms on metal surfaces, the lateral force component plays the dominant role. Furthermore, measuring spatial maps of the forces during manipulation yielded the full potential energy landscape of the tip-sample interaction.

In 1990, Eigler and Schweizer (1) positioned single Xe atoms with atomic-scale precision on a Ni(110) surface using a scanning tunneling microscope (STM). This technique of atom manipulation has subsequently been used to build model physical systems—such as quantum-confined structures (2, 3), magnetic nanostructures (4, 5), and artificial molecules (6, 7)—one atom at a time. In the most common STM manipulation technique, the adsorbate follows the tip by hopping from one surface binding site to the next, because a partial chemical bond is formed between the apex atom of the tip and the adsorbed atom or molecule. Previous studies of the manipulation process with STM (8, 9) were highly revealing but could not determine the forces involved in manipulation. Recently, the atomic force microscope (AFM) has been used to manipulate atoms at semiconducting surfaces (10), even at room temperature (11, 12). Atom manipulation with an AFM is particularly promising, because it allows the direct measurement of the required forces.

In this work, we used an AFM to quantify the forces required to pull individual adsorbates along a surface. We find that moving cobalt (Co) on Pt(111) requires a lateral force of 210 pN and that this force is independent of the vertical force. The lateral force can vary substantially with the chemical nature of the underlying surface as it is only 17 pN for Co on Cu(111). For both surfaces, the force on the tip due to the Co atom is nearly spherically symmetric. In contrast, for manipulating a carbon monoxide (CO) molecule, the forces are more complex, deviating markedly from spherical symmetry.

We used a frequency modulated AFM (13) with the qPlus sensor design (14) operating in ultrahigh vacuum at a temperature of ~5 K. A

metal tip was mounted on an oscillating cantilever (resonance frequency f_0 = 21,860 Hz) and used to probe the surface and move the adsorbates (Fig. 1A). The stiff cantilever (spring constant $k_0 \approx 1800$ Nm^{-1}) allows stable, small amplitude oscillation (A = 30 pm) close to the surface. We monitored the shift of the oscillation frequency Δf, which for small A is roughly proportional to the vertical stiffness $k_z \approx 2k_0/f_0 \times \Delta f$ of the tip-sample junction (13). To allow comparisons with STM manipulation experiments, we also detected the tunneling conductance G between tip and surface (15).

Figure 1, B to E, shows constant-height images of a single Co atom on Pt(111) and a single CO molecule on Cu(111) with tip heights close to the threshold for atom manipulation. In these images, k_z and G show circular symmetry, without any sign of the threefold substrate symmetry. The images obtained from Co on Pt(111) show a narrow dip in k_z and a peak in G. In contrast, the images from a CO molecule on Cu(111) have a more complex structure: k_z is flat around the central minimum, and G contains a central conductance peak within a broader conductance dip. For an asymmetric tip apex, k_z often deviates from circular symmetry for CO (16). In these images, the change in stiffness due to the adsorbate is 17 Nm^{-1} on Co and 9 Nm^{-1} on CO, in the range of a metal-metal bond stiffness (10 to 100 Nm^{-1}).

We can derive the force to move an atom from the measurement of k_z as a function of both vertical and lateral tip position. Figure 2 shows "line scans" obtained by moving the tip parallel to the surface at constant height, passing over the top of an isolated Co atom on Pt(111). These scans were repeated at progressively smaller tip heights until the Co atom hopped to a neighboring adsorption site, as illustrated in Fig. 2A. The direction of these scans corresponds to the direction of easiest motion on this substrate: It connects two neighboring threefold hollow adsorption sites. Figure 2, C and D, shows that both G and $|k_z|$ increased as the tip height was decreased. At the smallest tip height and at a lateral position about halfway to the adjacent binding site, a sudden jump occurred in both k_z and G. At this tip position, the Co atom reproducibly hopped from its initial binding site to the next and was

imaged again at its new position by the continuing line scan. In contrast, the atom reliably remained at its initial binding site when the tip was only 5 pm farther from the surface.

The vertical force F_z was determined by integrating k_z along z. The frequency shift, and therefore k_z, is an average of the tip-surface interaction over one oscillation cycle of the tip. This vertical blurring in all data was removed when computing F_z from k_z, by means of a deconvolution process (17).

We interpret F_z as the sum of two components: a background force F_B and the force F_z^* due to the presence of the adsorbate (Fig. 2B).
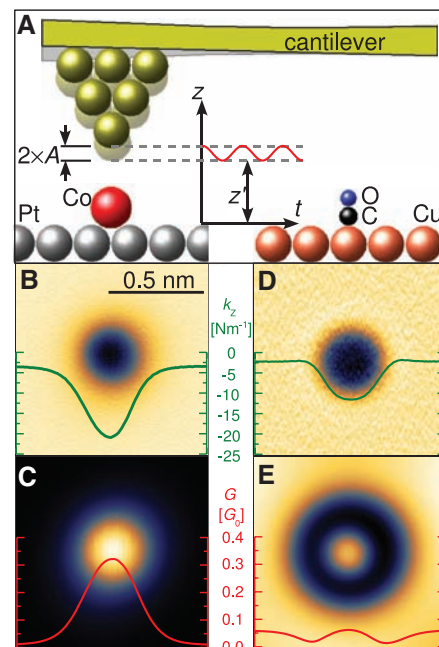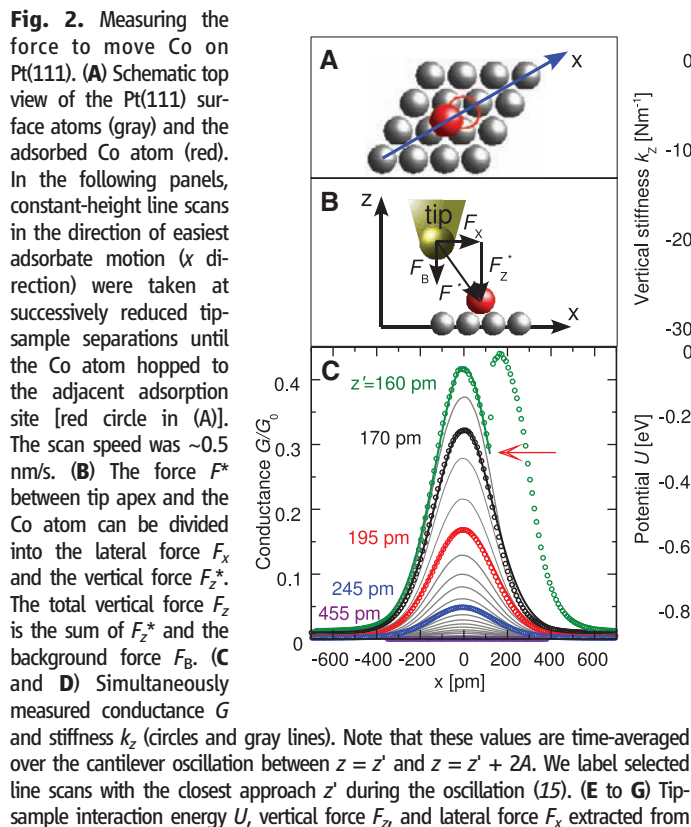

Fig. 1. Simultaneous AFM and STM measurements of individual adsorbates. (**A**) An atomically sharp metal tip is oscillating in z with an amplitude A = 30 pm over a flat metal surface on which an individual Co atom or CO molecule is adsorbed. The measured frequency shift of the cantilever from its natural resonance frequency is proportional to the vertical stiffness k_z of the tip-sample interaction. A small bias voltage of 1 mV was applied between tip and sample to measure the tunneling current, which is proportional to the conductance G, given in units of the single-channel, spin-degenerate quantum of conductance $G_0 = 2e^2/h = (12,906 \text{ ohm})^{-1}$, where e is the elementary charge and h is Planck's constant. The inset graph shows the tip motion $z(t)$ between its closest distance (z') and farthest distance ($z' + 2A$) from the sample. The ball models of the surfaces are scaled to match the dimensions of the images in the following panels. (**B** to **E**) Images measured at a constant height z' close to the threshold for adsorbate motion. (**B**) The tip-sample stiffness of a single Co atom on Pt(111). (**C**) Tip-sample conductance measured simultaneously for the same system as in (B). (**D** and **E**) Same as (B) and (C) for a single CO molecule on Cu(111). The colored curves in the panels are horizontal cross sections through the centers of the images.

[1]IBM Research Division, Almaden Research Center, 650 Harry Road, San Jose, CA 95120, USA. [2]Institute of Experimental and Applied Physics, University of Regensburg, D-93053 Regensburg, Germany.

*Present address: London Centre for Nanotechnology, Department of Physics and Astronomy, and Department of Chemistry, University College London, London WC1H 0AH, UK.
†To whom correspondence should be addressed. E-mail: markust@us.ibm.com

Fig. 2. Measuring the force to move Co on Pt(111). (**A**) Schematic top view of the Pt(111) surface atoms (gray) and the adsorbed Co atom (red). In the following panels, constant-height line scans in the direction of easiest adsorbate motion (x direction) were taken at successively reduced tip-sample separations until the Co atom hopped to the adjacent adsorption site [red circle in (A)]. The scan speed was ~0.5 nm/s. (**B**) The force F^* between tip apex and the Co atom can be divided into the lateral force F_x and the vertical force F_z^*. The total vertical force F_z is the sum of F_z^* and the background force F_B. (**C** and **D**) Simultaneously measured conductance G

and stiffness k_z (circles and gray lines). Note that these values are time-averaged over the cantilever oscillation between $z = z'$ and $z = z' + 2A$. We label selected line scans with the closest approach z' during the oscillation (15). (**E** to **G**) Tip-sample interaction energy U, vertical force F_z, and lateral force F_x extracted from the stiffness k_z data in (D). Selected line scans are labeled with the tip height z; here, the oscillation amplitude has been deconvolved from the curves. The red arrows in (C) to (G) indicate the hop of the Co atom to the neighboring binding site. Colored lines in (C), (F), and (G) are fits with the s-wave model.

The background force is in large part due to long-range (van der Waals) forces (18) and increases as the tip approaches the surface but does not depend on the lateral position. The vertical force F_z^* due to the adsorbate grows rapidly (Fig. 2F and fig. S3B), doubling in magnitude as z is changed by only 15 pm near the move threshold, indicating the short-range nature of this force.

We found the tip-sample interaction force to be nondissipative as long as the adsorbate did not hop to a new binding site (19). In this non-dissipative range of tip positions, we calculated the tip-sample interaction potential U (Fig. 2E) by integration of F_z along z (20). The lateral force F_x was then calculated by differentiation of U in the x direction (Fig. 2G). This technique allowed us to determine forces in any direction, even though the cantilever only senses the vertical stiffness. The lateral force was zero with the tip placed above the adsorbate, grew as the tip was moved laterally until a maximum was reached, and vanished far from the adsorbate.

This procedure allows us to determine the force that it takes to move a single Co atom across a Pt(111) surface. At the point where the atom hopped, we found a lateral force $F_x = 210 \pm 30$ pN (21). This force varied by only ±5% between different tips (22). At the same time, $F_z^* = -1.4 \pm 0.2$ nN was much larger than the lateral force and was nearly half as large as the bond-breaking force of 4 nN for a Pt point contact (23). To understand the interplay between the vertical and horizontal force components, we decreased z below the threshold height for hopping and

Fig. 3. Vertical and lateral forces for manipulating CO on Cu(111). Vertical (**A**) and lateral (**B**) force components when moving the tip over a CO molecule on Cu(111) for different tip heights z. The x direction corresponds to the easiest adsorbate motion from an on-top binding site to an adjacent one via a bridge site. The blue arrows mark a repulsive force $F_z^* = F_z - F_B$ of up to 20 pN between tip and molecule (see inset). At $z = 80$ pm, the molecule hopped between neighboring binding sites (red arrows). The green line in (B) is a linear fit to the lateral force with a slope of 1.2 N/m.

continued to measure the forces. We found that the lateral force to move the atom remained constant, whereas the vertical force varied by a large factor (figs. S1 and S2). For the range of heights measured, F_z^* at the point where the Co atom hopped varied from −0.45 nN (with the tip laterally far from the atom) to −3.0 nN (with the tip nearly above the atom). These results suggest that the lateral force is the key for the manipulation of
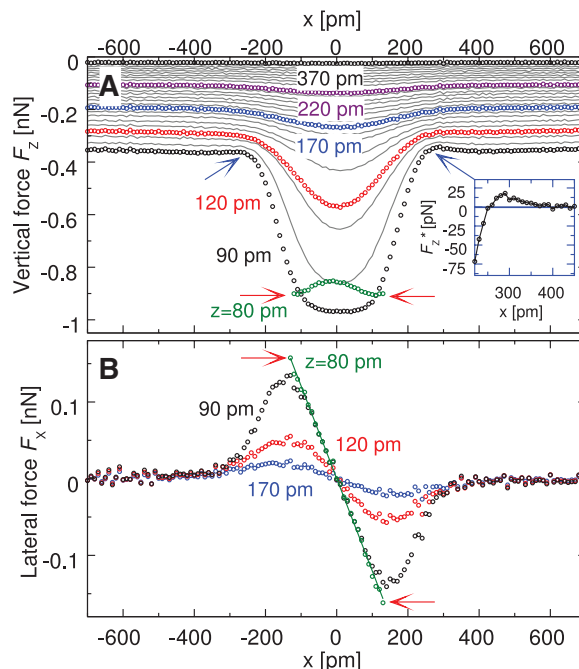
metal adsorbates on flat metal surfaces. This insensitivity to F_z^* is in contrast to the mechanism determined for moving Si atoms on Si(111) (12). There, it was found that the vertical force plays a dominant role by causing a reduction of the energy barrier between two adsorption sites as a result of relaxation of the Si adsorbate and surface.

The force that is required to move an atom strongly depends on the supporting substrate.
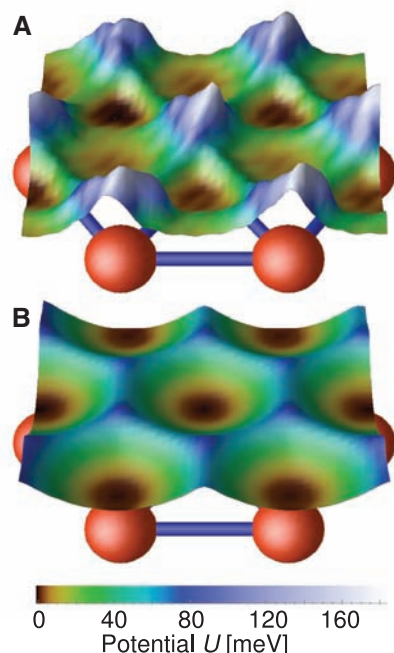
A

B

0   40   80   120   160
Potential U [meV]

Fig. 4. Tip-adsorbate energy landscape during manipulation. Two-dimensional potential landscapes of the tip-sample interaction energies during controlled manipulation of Co (**A**) and CO (**B**) on Cu(111). The energy scales of the color-coded images are shifted so that $U = 0$ at the preferred adsorption site for Co (fcc hollow site) and CO (on-top site). The underlying Cu(111) lattice is superimposed as a ball-and-stick model. The size of each image is 550×480 pm^2. (For more details, see fig. S5.)

Much smaller forces were sufficient to manipulate Co atoms on Cu(111) (fig. S3). Here, the required lateral force was only 17 ± 3 pN, even though Cu and Pt are both face-centered cubic (fcc) crystals and the Co atom binds at a threefold hollow site on both surfaces. This indicates that the nature of the chemical bonding plays a strong role. For Cu, the bonding is dominated by hybridization of the electronic states of the Co adsorbate with the $4s$ metal band, which shows no discernible direction dependence. In contrast, extra bonding occurs on Pt resulting from its partially filled and strongly directional $5d$ bonds (*24*), which apparently increase the forces necessary for manipulation.

To explore the spatial symmetry of the tip-adsorbate force, we modeled it as depending only on the tip-adsorbate distance [for details, see the supporting online material (SOM) text]. For this model, which is similar to the one suggested by Braun and Hla (*25*), the distance dependence of the force was derived from F_z^* measured at $x = 0$ (fig. S4). Despite the simplicity of this model, it agrees well with Co on Pt(111), as shown in Fig. 2, and with Co on Cu(111), as shown in fig. S3. This observed spherical symmetry of the force between the Co adsorbate and the tip apex suggests that the interaction occurs primarily via s-wave orbitals in both the tip-apex atom and the Co atom.

The manipulation forces for Co and a small molecule (CO) differed dramatically even though both adsorbates move on Cu(111) at a similar tunneling conductance in STM experiments (*8*). We found that the lateral manipulation force for CO molecules (160 ± 30 pN) is an order of magnitude larger than that for Co atoms (Fig. 3 and fig. S3). More importantly, the spatial dependence of the forces was markedly different. For example, F_z^* at closest tip-sample approach before hopping was almost independent of the lateral tip position around the center of the molecule and became repulsive at $x \approx \pm 300$ pm (Fig. 3). This dependence is in contrast to the s-wave nature of the forces that we found for metal adsorbates.

At small tip heights, the adsorbate follows the tip from binding site to binding site (*8, 9*). Under these conditions, maps of the forces and the tip-sample interaction potential can be constructed by combining k_z images obtained at various tip heights both above and below the manipulation threshold (*26*). Figure 4A shows this interaction potential for Co manipulated on Cu(111). The most stable adsorption sites are the fcc hollow sites (*9*), which appear as minima in the potential map. The neighboring hexagonal close-packed (hcp) sites have a slightly higher potential energy. We note that the Co atom can only be stabilized on this binding site when the tip is in close proximity (*9*). The fcc and hcp sites were separated by a potential barrier of 35 ± 5 meV, whereas the highest potential of 160 ± 30 meV occurred when the tip was placed above an on-top site of the surface. In contrast, in the potential landscape of Co on Pt(111), the barrier is 200 ± 30 meV and the two types of threefold hollow sites are essentially indistinguishable (fig. S5E). The potential landscape for an adsorbed CO molecule (Fig. 4B) clearly reflects the different symmetry of the binding site. In this case, we found that the bridge site had the lowest barrier (70 ± 10 meV) between two on-top binding sites.

For all three systems, the measured potential barrier height for positioning the tip between two neighboring adsorption sites is in close agreement with the diffusion barrier for adsorbate motion as determined by density functional theory [37 meV for Co on Cu(111)] (*27*) and experiments performed without the presence of a probe tip [75 meV for CO on Cu(111) (*28*) and 200 ± 10 meV for Co on Pt(111) (*29*)]. Although diffusion experiments detect the lowest barrier of the adsorbate-surface potential landscape without the presence of a tip, our measurements determine the potential for moving the tip resulting from all interactions among tip, surface, and adsorbate.

The present method for measuring the full tip-sample potential landscape and the forces necessary to manipulate atoms and molecules in arbitrary directions provides important information about the manipulation process without relying on advanced simulations such as density functional theory. It could give additional impetus to the exploration of atomic-scale friction and atom and molecule diffusion on surfaces and

offer a deeper insight into controlled bottom-up assembly mechanisms. A systematic investigation of the manipulation forces on different surface-adsorbate combinations is now possible, and the driving mechanism to create future nanoscale devices can be explored in a quantitative manner.

References and Notes
1. D. M. Eigler, E. K. Schweizer, *Nature* **344**, 524 (1990).
2. M. F. Crommie, C. P. Lutz, D. M. Eigler, *Science* **262**, 218 (1993).
3. N. Nilius, T. M. Wallis, W. Ho, *Science* **297**, 1853 (2002).
4. W. Chen, T. Jamneala, V. Madhavan, M. F. Crommie, *Phys. Rev. B* **60**, R8529 (1999).
5. C. F. Hirjibehedin, C. P. Lutz, A. J. Heinrich, *Science* **312**, 1021 (2006).
6. S.-W. Hla, L. Bartels, G. Meyer, K.-H. Rieder, *Phys. Rev. Lett.* **85**, 2777 (2000).
7. R. Yamachika, M. Grobis, A. Wachowiak, M. F. Crommie, *Science* **304**, 281 (2004).
8. L. Bartels, G. Meyer, K.-H. Rieder, *Phys. Rev. Lett.* **79**, 697 (1997).
9. J. A. Stroscio, R. J. Celotta, *Science* **306**, 242 (2004).
10. N. Oyabu, Y. Sugimoto, M. Abe, Ó. Custance, S. Morita, *Nanotechnology* **16**, S112 (2005).
11. Y. Sugimoto et al., *Nat. Mater.* **4**, 156 (2005).
12. Y. Sugimoto et al., *Phys. Rev. Lett.* **98**, 106104 (2007).
13. T. R. Albrecht, P. Grütter, D. Horne, D. Rugar, *J. Appl. Phys.* **69**, 668 (1991).
14. F. J. Giessibl, *Appl. Phys. Lett.* **76**, 1470 (2000).
15. Detecting G allows us to assign $z = 0$ throughout this work as the extrapolated tip height, where the conductance to the bare surface is equal to G_0 (fig. S3A). This approach provides a convenient reference for z, which corresponds roughly to the point contact between the tip and the bare surface. This assignment does not necessarily provide direct comparison of the tip heights between the two surfaces explored in this work. The measured conductance is an average over the tip oscillation. For the amplitude $A = 30$ pm used here, the conductance differs by only ~11% from the value of a nonoscillating tip at the same mean height.
16. F. J. Giessibl, S. Hembacher, H. Bielefeld, J. Mannhart, *Science* **289**, 422 (2000).
17. J. E. Sader, S. P. Jarvis, *Appl. Phys. Lett.* **84**, 1801 (2004).
18. S. Morita, R. Wiesendanger, E. Meyer, Eds. *Noncontact Atomic Force Microscopy* (Springer, Berlin, 2002).
19. We corroborate this assumption with measurements of the power dissipation. Dissipative components in the tip-sample interaction cause an increase in the power required to maintain a constant oscillation amplitude. In our experiment, the energy stored in the mechanical motion of the tip is only $E = \frac{1}{2}k_0 A^2 \approx$ 5 eV. The cantilever has a mechanical quality factor of $Q \approx 35,000$, so that the intrinsic energy loss per oscillation cycle $[= 2\pi E/Q$, see (*18*)] is less than 1 meV. Therefore, we estimate that the dissipative interaction between tip and sample is less than 1% of the typical conservative interaction, so it can be safely neglected; see fig. S5 for more information.
20. H. Hölscher, S. M. Langkat, A. Schwarz, R. Wiesendanger, *Appl. Phys. Lett.* **81**, 4428 (2002).
21. The ±10% uncertainty of the cantilever stiffness produces a systematic error. In addition, the uncertainties given in the text include the error due to the finite tip-height increments (±10%) and the effect that different tips (*22*) produce slightly different results (±5%).
22. Throughout this work, we refer to a changed atomic arrangement at the tip apex (e.g., by touching the tip to the surface) as a different tip.
23. S. R. Bahn, K. W. Jacobsen, *Phys. Rev. Lett.* **87**, 266101 (2001).
24. B. Hammer, J. K. Nørskov, *Nature* **376**, 238 (1995).
25. K.-F. Braun, S.-W. Hla, *Phys. Rev. B* **75**, 033406 (2007).
26. For each lateral tip position, the k_z images for heights above the manipulation threshold were laterally shifted to the location of the binding site nearest the tip. Because dissipation occurred when the atom hopped, comparison of energies between different binding sites might not be valid, but energies within the basin around any one binding site are correct. For more details, see fig. S5.

27. D. V. Tsivlin, V. S. Stepanyuk, W. Hergert, J. Kirschner, *Phys. Rev. B* **68**, 205411 (2003).
28. K. L. Wong, B. V. Rao, G. Pawin, E. Ulin-Avila, L. Bartels, *J. Chem. Phys.* **123**, 201102 (2005).
29. P. Buluschek, thesis, École Polytechnique Fédéral de Lausanne, Switzerland (2007).

Bioinspired Design and Assembly of Platelet Reinforced Polymer Films

Lorenz J. Bonderer, André R. Studart,*† Ludwig J. Gauckler†

Although strong and stiff human-made composites have long been developed, the microstructure of today's most advanced composites has yet to achieve the order and sophisticated hierarchy of hybrid materials built up by living organisms in nature. Clay-based nanocomposites with layered structure can reach notable stiffness and strength, but these properties are usually not accompanied by the ductility and flaw tolerance found in the structures generated by natural hybrid materials. By using principles found in natural composites, we showed that layered hybrid films combining high tensile strength and ductile behavior can be obtained through the bottom-up colloidal assembly of strong submicrometer-thick ceramic platelets within a ductile polymer matrix.

Steel and other metal alloys have long been used for the fabrication of strong and flaw-tolerant materials for structural applications. As opposed to metals, ceramic and polymeric materials do not exhibit the unique combination of high strength and flaw tolerance. Ceramics are typically strong but not tolerant to surface flaws and cracks, whereas most polymers are flaw-tolerant but deform extensively at rather low applied stresses.

Nature has found its way around this dilemma by combining plateletlike ceramic building blocks with polymeric matrices to render hybrid materials that are both strong and flaw-tolerant. Examples include mineralized tissues of vertebrates, such as bone, teeth, and calcified tendons, as well as the outer skeleton of invertebrates, such as the nacreous layer of mollusk shells (*1*).

The exquisite structure of these biological materials and the underlying concepts leading to their mechanical behavior have been extensively studied (*2–5*). Although substantial progress has been made on understanding the mechanical response of such structures (*6–11*), the manufacture of artificial composites that copy nature's designs remains a challenging goal.

A number of different materials have been used as inorganic reinforcing platelets for the fabrication of polymer-matrix artificial composites, including glass, graphite, SiC, AlB₂, mica, talc, and clays (*12–15*). Considerable increase in stiffness and strength has been achieved at rather low platelet concentrations, particularly in the case of polymers reinforced with nanosized clay

particles (*16*). However, improvements in the composite strength at higher platelet concentrations [>10 weight % (wt %)] are often notably lower than that expected from theoretical models for reinforced polymers (*12, 17, 18*). This has been attributed to difficulties in achieving complete exfoliation and dispersion of platelets within the organic matrix and to poor bonding at the inorganic-organic interface (*12, 18, 19*). The strengthening seen with nanosized clay particles also seems to involve the cross-linking of polymer chains between neighboring platelets rather than solely depending on load transfer mechanisms operative in composites reinforced with micrometer-sized inorganic fibers (*17, 18, 20*). This cross-linking effect was used in making clay-based nanocomposites exhibiting tensile strength up to 400 MPa (*18*). However, such strong nanocomposites exhibit brittle fracture under tension (flaw intolerance), presumably because of the very high platelet concentration [50 volume % (vol %)] needed to reach this high strength level.

We applied some of the structural concepts found in biological materials to design and fabricate platelet-reinforced hybrid films that are both strong and ductile. The size and aspect ratio of the reinforcing platelets, as well as the mechanical properties of the individual inorganic and organic phases, were deliberately chosen to mimic the designing principles of strong and tough biological structures.

Biological materials such as bones, teeth, and mollusk shells are characterized by a layered structure consisting of strong inorganic platelets embedded in a soft, ductile organic matrix (*1*). In spite of the inherently weak inorganic constituents (e.g., silica, calcium carbonates, and phosphates), the high strength of the inorganic building blocks is ensured by limiting at least one of their dimensions to the nanoscale (*3*). These tiny building blocks

are usually organized into a hierarchical structure spanning over various length scales. Changes in the fraction of inorganic phase (i.e., degree of mineralization) lead to hybrid materials ranging from soft tissues such as calcified tendons to strong, hard structures such as bone and nacre. Among the different models that have been proposed to describe the mechanical response of biological mineralized structures (*8–11*), a simple approach based on the mechanics of composite structures has been successfully applied to explain the strength and ductility of nacre (*7*).

The strength of nacre has been described on the basis of a simple shear lag model, according to which the applied load is transferred to the inorganic platelets through shear stresses developed in the organic matrix (*7*). For ductile matrices exhibiting a yield shear strength τ_y and a perfect bonding to the platelet surface (interfacial strength $\tau_i \geq \tau_y$), the ultimate tensile strength of the hybrid material (σ_c) can be estimated from the volume fraction of platelets (V_p), the platelet aspect ratio (s), and the tensile strength of the platelets (σ_p) and of the organic matrix (σ_m), as follows (*21*):

$$\sigma_c = \alpha V_p \sigma_p + (1 - V_p)\sigma_m \qquad (1)$$

with the factor α being a function of s, τ_y, and σ_p.

The tensile strength of the hybrid material depends on the operative failure mode, which in turn is determined by the aspect ratio of the inorganic platelets, s. For aspect ratios higher than a critical value ($s > s_c$), the composite fails because of the fracture of platelets (Fig. 1A), leading to a brittle catastrophic rupture of the material. In this case ($s > s_c$), the factor α in Eq. 1 is given by the following relation:

$$\alpha = 1 - \frac{\sigma_p}{2\tau_y s} \qquad (2)$$

On the other hand, for aspect ratios lower than the critical condition ($s < s_c$) the continuous matrix yields before the platelets break, thus leading to toughening mechanisms such as platelet pull-out and matrix plastic flow before the complete rupture of the composite (Fig. 1A). For $s < s_c$, the factor α reads

$$\alpha = \frac{\tau_y s}{2\sigma_p} \qquad (3)$$

Composites that fail under the platelet fracture mode are strong but brittle and thus flaw-intolerant, whereas materials that rupture under the platelet pull-out mode are generally weak but ductile and thus flaw-tolerant (Fig. 1A). Note that for weak inorganic-organic interfaces fracture occurs at the interface before the matrix

Department of Materials, Eidgenössische Technische Hochschule (ETH)–Zürich, 8093 Zürich, Switzerland.

*Present address: Experimental Soft Condensed Matter Group, Department of Physics, School of Engineering and Applied Sciences, Harvard University, Cambridge, MA 02138, USA.
†To whom correspondence should be addressed. E-mail: studart@seas.harvard.edu (A.R.S.); ludwig.gauckler@mat.ethz.ch (L.J.G.)